Continuum Mech. Thermodyn. (2024) 36:1109–1127
https://doi.org/10.1007/s00161-023-01228-6

ORIGINAL ARTICLE

Guifeng Wang · Fan Shi · Zhenyu Chen · Yue Yu · C. W. Lim

Controllable flexural wave bandgap in extensible metamaterial beams with embedded multiple resonators

Received: 11 April 2022 / Accepted: 3 May 2023 / Published online: 24 May 2023

Abstract The interest in phononic crystals and acoustic metamaterials has been an intensive subject of research in recent years. Finding a robust way to significantly expand or actively control the bandgap has received extensive attention. In this study, we propose a prestressed metamaterial beam attached with multiply local resonators connected by actively tunable piezoelectric springs. The Euler–Bernoulli beam theory and Timoshenko beam theory are applied in the theoretical analysis of the system. Further, the spectral element method is utilized to analytically compute the dispersion relation and transmission ratio and excellent agreement with reference to the benchmark is reported. The influences of an external axial force on the bandgap range and attenuation behavior are further studied. Subsequently, the effect of resonator number and mass on the local resonance bandgap structure is investigated in two parametric studies. The active control of bandgap range and frequency is then verified. By analyzing frequency response function, the tunable transmission ratio of a supercell can be observed. To conclude, this paper not only provides a guideline for designs of wave attenuation with multiple frequency regimes in a one-dimensional system, but it can also be extended to sub-wavelength wave manipulation designs.

Keywords Active control · Euler–Bernoulli beam · Local resonance · Spectral element · Timoshenko beam · Wave attenuation

1 Introduction

Structural vibration, one of the most common mechanical motions in daily life, seriously affects the serviceability of a structure or even possibly causes serious damage [1]. For instance, the continuous vibration caused

Communicated by Andreas Öchsner.

G. Wang · C. W. Lim (✉)
Department of Architecture and Civil Engineering, City University of Hong Kong, Tat Chee Avenue, Kowloon, Hong Kong SAR, People's Republic of China
E-mail: bccwlim@cityu.edu.hk

F. Shi · Z. Chen (✉)
Department of Mechanical and Aerospace Engineering, The Hong Kong University of Science and Technology, Clear Water Bay, Kowloon, Hong Kong SAR, People's Republic of China
E-mail: maezhenychen@ust.hk

Y. Yu
School of Science, Nantong University, Nantong 226019, People's Republic of China

C. W. Lim
City University of Hong Kong Shenzhen Research Institute, Shenzhen 518057, People's Republic of China

by subway systems may lead to fatigue damage to surrounding buildings [2,3] and irreversible damage to precision facilities [4], although the vibration amplitude may not be large. Therefore, vibration isolation or suppression has received extensive attention in the past. To this end, the birth of phononic crystals (PnCs) and acoustic metamaterials (AMs) provides new ideas for vibration and noise control. PnC is a kind of structure constructed by periodically arranged materials [5], structures [6], and/or periodic boundary conditions [7,8]. But PnC is limited with its size, and hence, it is not practicable for generating low frequency bandgaps in real engineering works. AMs which consist of materials and structures with local resonance (LR) were then proposed [9]. Li and Chan [10] introduced double-negative AMs by dispersing soft rubber into water, and the new structure shows many peculiar properties like negative refraction [11–13], negative bulk modulus [14,15], quasi-zero stiffness [16,17], etc. Consequently, AMs have attracted increasing research interests for their potential engineering applications such as waveguiding [18–20], wave attenuation [21], wave filtering [22], sound barriers [23], and vibration control [24].

Band structure is one of the most important properties of AMs [25,26]. Generally, the band structure that indicates the relation between frequency and wavenumber consists of two parts: passband and bandgap. Elastic waves travel freely in the passband range, while the propagation of elastic waves is prohibited in the bandgap range [27]. Based on the generation mechanism, bandgaps can be further divided into two types: Bragg scattering bandgap (BSBG) [28–30] and local resonance bandgap (LRBG) [31–33]. BSBG results from wave destructive behavior between the forward and backward waves propagating through neighboring unit cells [34], and it has the advantage of strong attenuation performance and wide bandgap [35]. However, due to the strong dependence on the shapes of scatters and lattice symmetry, BSBG is not robust [36]. Moreover, BSBG is usually applied at a frequency range corresponding to a wavelength comparable to the lattice constant [37], which means a sufficiently large-scale structure is necessary if low frequency BSBG is desired by engineers. But the structural size in real engineering construction is usually strictly controlled and thus, it strongly restricts the application of PnCs based on the Bragg scattering mechanism. To overcome this limitation, Liu et al. [9] first introduced a LR type AM by embedding lead local resonator into silicon rubber matrix. It was reported that the corresponding wavelength of bandgap is two orders of magnitude larger than the lattice constant. Since then, various structures and systems based on local resonance that can generate low frequency bandgaps were proposed. For instance, Chang et al. [21] proposed a one-dimensional (1D) spring-mass model with longitudinal local resonant substructure. Chen et al. [33] introduced a novel 2D structure by periodically arranging cylinders in sinusoidal-shaped ligaments, which is able to establish an elastic waveguide within a subwavelength frequency region.

Engineering structures can be utilized to design PnCs and AMs, and beam is one of the most popular structural element in this regard. One advantage of beam-type AMs in real engineering applications is its role in vibration suppression. Using LR type AMs, Wang et al. [38] designed an LR beam by periodically attaching cuprum-rubber oscillators on a single duralumin beam. They showed that LRBG exists in this beam system by both theoretical and experimental approaches with the appearance of the structural periodicity induced BSBG. Later, Liu et al. [39] designed a simplified LR beam model with the resonator composed of a concentrated mass and an ideal massless spring. This is a single degree of freedom (SDOF) resonator. Subsequently, various studies with more complicated models were proposed [40,41,43]. Specifically, Casalotti et al. [44] proposed embedded nonlinear vibration absorbers on a homogenous beam and wave attenuation performance could be improved by tuning nonlinear vibration absorbers optimally. However, most of the LR beams mainly focused on SDOF resonator. Thus, Hu et al. [45], Huang and Sun [46], and Li et al. [47] investigated the dispersion relation of a homogenous beam attached with multiple degrees of freedom (MDOF) resonators and they found lower frequency bandgaps can be generated by increasing number of resonators.

One of the main drawbacks of AMs is the narrow bandgap width [48,49]. In the past few years, numerous methods to tune bandgaps of AMs were proposed, such as temperature [50], electric fields [51], magnetic fields [52], and applied mechanical load [53] as the key choices. Zhou et al. [54] employed smart resonators which comprised lumped masses and piezoelectric springs with tunable stiffness. The width and frequency range of an LRBG can be actively controlled by tuning the linear spring constant. However, the complicated technology features raise manufacturing and maintaining costs and, hence, more robust solutions are desired. Yuan et al. [55] applied a longitudinal tensile force on an LR beam made of aluminum alloy, and they verified by numerical analysis and experiment that an axial tensile force can efficiently tune BSBG. Moreover, a new idea of attaching graded local resonators also attracts great research attention. For example, Hu et al. [56] employed several local resonators with the same masses but different natural frequencies on the host beam, which resulted in 150% enlargement of the wave attenuation range.

All previous designs on LR beam attached with MDOF resonators mainly focused on the multiple LRBGs generated by MDOF resonators and passive control of bandgaps. In this paper, a comprehensive study on an active controllable MDOF LR beam with actively controllable piezoelectric springs and the system is subjected to an axial tensile force. The passive control via tuning axial force and active control via tuning piezoelectric spring stiffness are achieved simultaneously. The beam system is attached with MDOF local resonators with piezoelectric springs. The governing equation of motion is firstly derived by using the Euler–Bernoulli beam theory and Timoshenko beam theory. Subsequently, spectral element method (SEM) is used to solve the dispersion relation and transmission ratio. Excellent agreement between the two solution methods is observed, and it is further validated with benchmark data. The effect of axial force on bandgap range and attenuation coefficient is studied. It is shown that axial force has a dramatic effect on the bandgap range of BSBG and the attenuation coefficient of LRBGs. In addition, two parametric studies by controlling the number of resonators and the total resonator masses are conducted to investigate the primary factor that controls the total LRBG width and starting frequency of LRBG. Further, tunability of LRBG and BSBG is demonstrated again by tuning the piezoelectric spring stiffness. The analytical transmission curve is then determined by introducing an excitation on the right end and setting a signal receiver at the left end. The result indicates that flexural wave propagation can be efficiently prohibited in the bandgap range. This result has great application potential in beam vibration isolation and suppression.

2 Modeling and theoretical derivation

The beam system studied herein is a prestressed beam with periodic attachment of SDOF or MDOF resonators. Shown in Fig. 1a is an infinitely long homogenous beam with width b in the OY direction and thickness h in the OZ direction. The beam is subjected to an axial force P and is attached with periodic arrays of resonators. The beam model can be treated as an array of infinite unit cells, and one representative unit cell with length a is shown by the red dash frame in Fig. 1a. As the system periodicity is in the OX direction, a view of the beam system in the XOZ plane is shown in Fig. 1b. Periodicity of the superstructure can be observed in the OX direction. One typical unit cell with a total of n massless springs and n resonators attached to the beam element is presented in Fig. 1c, with each spring constant in the system denoted as k_i, while the mass of resonator is m_i, where $i = 1, 2, \ldots, n$. A simplified analytical model is presented in Fig. 1d. In this study, linear piezoelectric springs are assumed and the total stiffness can be expressed as [57]

$$k_i = k_{i,a} + k_{i,p} \tag{1}$$

where $k_{i,a}$ is the active stiffness due to the control gain while $k_{i,p}$ is the original passive structural stiffness of the spring.

2.1 Euler–Bernoulli beam theory

To begin with, the Euler–Bernoulli beam theory and Timoshenko beam theory are adopted to derive the governing equation of motion. SEM is subsequently applied to determine the dispersion relation and transmission ratio. The system governing equation of motion using the Euler–Bernoulli beam theory, which neglects rotary inertia and shear deformation, gives the formula of an extensible beam as [58]

$$\mathrm{EI}\frac{\mathrm{d}^4 w\,(x)}{\mathrm{d}x^4} - P\frac{\mathrm{d}^2 w\,(x)}{\mathrm{d}x^2} - \rho S\omega^2 w\,(x) = 0 \tag{2}$$

where E is Young's modulus (Pa), $I = bh^3/12$ is second moment of area (m^4) referring to the neutral axis of the beam, P is axial tensile force (N), ρ is mass density ($\mathrm{kg/m}^3$), S is cross-sectional area (m^2), $w\,(x, t)$ is flexural deflection, ω is the angular frequency.

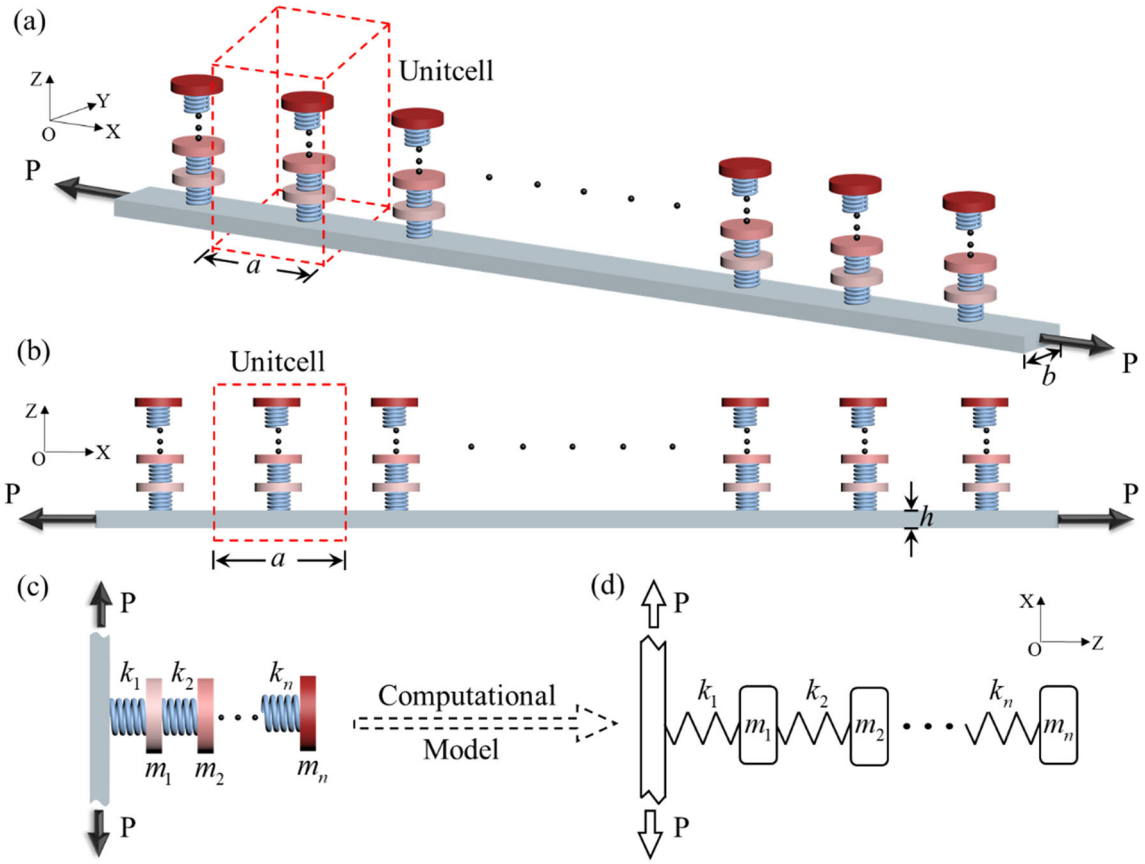

Fig. 1 **a** 3D schematic illustration of a prestressed MDOF LR beam. **b** Front view of the beam system in the XOZ plane. **c** Front view of one unit cell in the ZOX plane. **d** Analytical model of a unit cell (color figure online)

Based on Newton's second law of motion, the governing equations of resonators in an assembled matrix format as

$$-\omega^2 \begin{bmatrix} m_1 u_1 \\ m_2 u_2 \\ \vdots \\ \vdots \\ m_{n-1} u_{n-1} \\ m_n u_n \end{bmatrix} = \begin{bmatrix} k_1 & -k_1-k_2 & k_2 & 0 & \dots & \dots & 0 \\ 0 & k_2 & -k_2-k_3 & k_3 & 0 & \dots & 0 \\ \vdots & \vdots & \ddots & \ddots & \ddots & \vdots & \vdots \\ \vdots & \vdots & \ddots & \ddots & \ddots & \vdots & \vdots \\ 0 & 0 & \dots & 0 & k_{n-1} & -k_{n-1}-k_n & k_n \\ 0 & 0 & \dots & \dots & 0 & k_n & -k_n \end{bmatrix} \begin{bmatrix} w \\ u_1 \\ u_2 \\ \vdots \\ \vdots \\ u_{n-1} \\ u_n \end{bmatrix} \tag{3}$$

where m_n, k_n, and u_n are the mass, spring stiffness, and transverse displacement of the n-th resonator, respectively.

By assuming the interaction force between beam and the first resonator be $f_j = k_1 (w - u_1)$ and with the help of Eq. (3), f_j is further expressed as

$$f_j = D_{\mathrm{R}} w \tag{4}$$

where $D_{\mathrm{R}} = \left(k_1 k_2 - k_1 k_2 \eta - k_1 m_1 \omega^2\right) / \left(k_1 - k_2 \eta + k_2 - m_1 \omega^2\right)$ and η is a reference parameter related to k_i $(i = 2, \dots, n-1, n)$, ω, and m_i $(i = 2, \dots, n-1, n)$. It should be noted that η depends on the size of Eq. (3) because it is obtained by decoupling u_i $(i = 1, 2, \dots, n-1, n)$ from the last row of Eq. (3) to the first row. For example, $\eta = k_2 / \left(k_2 - \omega^2 m_2\right)$ for $n = 2$ and $\eta = 1 \Big/ \left(1 - \frac{k_3^2}{k_3 k_2 - \omega^2 m_3 k_2} + \frac{k_3}{k_2} - \frac{m_2 \omega^2}{k_2}\right)$ for $n = 3$.

The harmonic solution of Eq. (2) is $w(x) = A_{\mathrm{E}} e^{i\xi_{\mathrm{E}} x}$ [59]. Thus, Eq. (2) can be expressed as

$$\mathrm{EI}\xi_{\mathrm{E}}^4 + P\xi_{\mathrm{E}}^2 - \rho S\omega^2 = 0 \tag{5}$$

It is noted that the solutions to Eq. (5) $\xi_{\mathrm{E},\mathrm{I}}$ $(I = 1,\ 2,\ 3,\ 4)$ take the form

$$\xi_{\mathrm{E},1} = -\xi_{\mathrm{E},2} = \sqrt{\frac{-P + \sqrt{P^2 + 4\mathrm{EI}\rho S\omega^2}}{2\mathrm{EI}}} \tag{6a}$$

$$\xi_{\mathrm{E},3} = -\xi_{\mathrm{E},4} = \sqrt{\frac{-P - \sqrt{P^2 + 4\mathrm{EI}\rho S\omega^2}}{2\mathrm{EI}}} \tag{6b}$$

and the general solution of Eq. (2) is

$$w(x) = A_{\mathrm{E},1} e^{i\xi_{\mathrm{E},1}x} + A_{\mathrm{E},2} e^{i\xi_{\mathrm{E},2}x} + A_{\mathrm{E},3} e^{i\xi_{\mathrm{E},3}x} + A_{\mathrm{E},4} e^{i\xi_{\mathrm{E},4}x} \tag{7}$$

According to Euler beam theory, we have $\theta(x) = w'(x)$, $M(x) = -\mathrm{EI}w''(x)$, and $Q(x) = -\mathrm{EI}w'''(x)$. Based on beam continuity and resonator effects, the physical parameters of each neighboring unit cell have the relation below

$$w_{j+1}(0) = w_j(a) \tag{8}$$

$$\theta_{j+1}(0) = \theta_j(a) \tag{9}$$

$$M_{j+1}(0) = M_j(a) \tag{10}$$

$$Q_{j+1}(0) = Q_j(a) + D_{\mathrm{R}} w_j(a) \tag{11}$$

where subscript j denotes the j-th unit cell.

We further introduce a local nodal displacement vector $\mathbf{p} = (\mathbf{p_1}\ \ \mathbf{p_2})^{\mathrm{T}}$, where $\mathbf{p_1} = \left(w_j(0)\ \theta_j(0)\right)$ and $\mathbf{p_2} = \left(w_{j+1}(0)\ \theta_{j+1}(0)\right)$. Based on Eqs. (8) and (9), we obtain

$$\mathbf{p} = \mathbf{U}_{\mathrm{E}}\mathbf{A}_{\mathrm{E}} \tag{12}$$

where

$$\mathbf{U}_{\mathrm{E}} = \begin{bmatrix} 1 & 1 & 1 & 1 \\ i\xi_{\mathrm{E},1} & i\xi_{\mathrm{E},2} & i\xi_{\mathrm{E},3} & i\xi_{\mathrm{E},4} \\ e^{i\xi_{\mathrm{E},1}a} & e^{i\xi_{\mathrm{E},2}a} & e^{i\xi_{\mathrm{E},3}a} & e^{i\xi_{\mathrm{E},4}a} \\ i\xi_{\mathrm{E},1}e^{i\xi_{\mathrm{E},1}a} & i\xi_{\mathrm{E},2}e^{i\xi_{\mathrm{E},2}a} & i\xi_{\mathrm{E},3}e^{i\xi_{\mathrm{E},3}a} & i\xi_{\mathrm{E},4}e^{i\xi_{\mathrm{E},4}a} \end{bmatrix} \tag{13}$$

and

$$\mathbf{A}_{\mathrm{E}} = \left[A_{\mathrm{E},1}\ A_{\mathrm{E},2}\ A_{\mathrm{E},3}\ A_{\mathrm{E},4}\right]^{\mathrm{T}} \tag{14}$$

Besides, the local nodal force vector is $\mathbf{f} = \left(\mathbf{f_1}\ \mathbf{f_2}\right)^{\mathrm{T}}$, where $\mathbf{f_1} = \left(-M_j(0)\ -Q_j(0)\right)$ and $\mathbf{f_2} = \left(M_{j+1}(0)\ Q_{j+1}(0)\right)$. Referring to Eqs. (10) and (11), we have

$$\mathbf{f} = \mathbf{V}_{\mathrm{E}}\mathbf{A}_{\mathrm{E}} \tag{15}$$

where

$$\mathbf{V}_{\mathrm{E}} = \mathrm{EI}\begin{bmatrix} -\left(\xi_{\mathrm{E},1}\right)^2 & -\left(\xi_{\mathrm{E},2}\right)^2 & -\left(\xi_{\mathrm{E},3}\right)^2 & -\left(\xi_{\mathrm{E},4}\right)^2 \\ -i\left(\xi_{\mathrm{E},1}\right)^3 & -i\left(\xi_{\mathrm{E},2}\right)^3 & -i\left(\xi_{\mathrm{E},3}\right)^3 & -i\left(\xi_{\mathrm{E},4}\right)^3 \\ \left(\xi_{\mathrm{E},1}\right)^2 e^{i\xi_{\mathrm{E},1}a} & \left(\xi_{\mathrm{E},2}\right)^2 e^{i\xi_{\mathrm{E},2}a} & \left(\xi_{\mathrm{E},3}\right)^2 e^{i\xi_{\mathrm{E},3}a} & \left(\xi_{\mathrm{E},4}\right)^2 e^{i\xi_{\mathrm{E},4}a} \\ \left(i\left(\xi_{\mathrm{E},1}\right)^3 + \frac{D_{\mathrm{R}}}{\mathrm{EI}}\right) e^{i\xi_{\mathrm{E},1}a} & \left(i\left(\xi_{\mathrm{E},2}\right)^3 + \frac{D_{\mathrm{R}}}{\mathrm{EI}}\right) e^{i\xi_{\mathrm{E},2}a} & \left(i\left(\xi_{\mathrm{E},3}\right)^3 + \frac{D_{\mathrm{R}}}{\mathrm{EI}}\right) e^{i\xi_{\mathrm{E},3}a} & \left(i\left(\xi_{\mathrm{E},4}\right)^3 + \frac{D_{\mathrm{R}}}{\mathrm{EI}}\right) e^{i\xi_{\mathrm{E},4}a} \end{bmatrix} \tag{16}$$

Combining Eqs. (12) and (15) yields

$$\begin{pmatrix} \mathbf{f}_1 \\ \mathbf{f}_2 \end{pmatrix} = \mathbf{M}_{\mathrm{E}} \begin{pmatrix} \mathbf{p}_1 \\ \mathbf{p}_2 \end{pmatrix} \tag{17}$$

where the dynamic stiffness matrix $\mathbf{M}_{\mathrm{E}}$ can be expressed as

$$\mathbf{M}_{\mathrm{E}} = \begin{bmatrix} \mathbf{M}_{\mathrm{E,LL}} & \mathbf{M}_{\mathrm{E,LR}} \\ \mathbf{M}_{\mathrm{E,RL}} & \mathbf{M}_{\mathrm{E,RR}} \end{bmatrix} = \mathbf{V}_{\mathrm{E}}\mathbf{U}_{\mathrm{E}}^{-1} \tag{18}$$

Because of structural periodicity, the Bloch theorem can be applied. Then, the physical parameters at the left end of each unit cell can be expressed as

$$\mathbf{p}_2 = e^{\mathrm{ika}}\mathbf{p}_1, \quad \mathbf{f}_2 = -e^{\mathrm{ika}}\mathbf{f}_1 \tag{19}$$

where k is the Bloch wave vector.

By Eqs. (17) and (19), we can generalize a standard eigenvalue equation as below to solve the Bloch wave vector k

$$\begin{bmatrix} \mathbf{0} & \mathbf{I} \\ -\mathbf{M}_{\mathrm{E,LR}}^{-1}\mathbf{M}_{\mathrm{E,RL}} & -\mathbf{M}_{\mathrm{E,LR}}^{-1}\left(\mathbf{M}_{\mathrm{E,LL}} + \mathbf{M}_{\mathrm{E,RR}}\right) \end{bmatrix} \begin{pmatrix} \mathbf{p}_1 \\ e^{\mathrm{ika}}\mathbf{p}_1 \end{pmatrix} - e^{\mathrm{ika}} \begin{pmatrix} \mathbf{p}_1 \\ e^{\mathrm{ika}}\mathbf{p}_1 \end{pmatrix} = 0 \tag{20}$$

Because the coefficient matrix in Eq. (20) is a 4×4 matrix, it is evident that Eq. (20) has four complex roots, assumed as $p + qi$, for any given frequencyω. For an arbitrary complex root, we further assume that the corresponding complex Bloch wave number k can be expressed as $k = c + di$. Thus, for the eigenvalue problem in Eq. (20), we have

$$d = -\ln\left(p^2 + q^2\right)/(2a) \tag{21}$$

and

$$c = \begin{cases} \arctan\left(q/p\right)/a & \text{if } p > 0 \\ \left[\pi + \arctan\left(q/p\right)\right]/a & \text{if } p < 0 \text{ and } q > 0 \\ \left[-\pi + \arctan\left(q/p\right)\right]/a & \text{if } p < 0 \text{ and } q < 0 \end{cases} \tag{22}$$

We consider the propagation of flexural wave in a beam system composed of N unit cells. An external signal is excited at the right-end, and the response is received at the left-end. The beam vibration can be expressed in the form of a global dynamic stiffness equation as

$$\mathbf{f}_{\mathrm{tot}} = \mathbf{M}_{\mathrm{E,tot}}\,\mathbf{p}_{\mathrm{tot}} \tag{23}$$

where $\mathbf{f}_{\mathrm{tot}}$, $\mathbf{p}_{\mathrm{tot}}$, and $\mathbf{M}_{\mathrm{E,tot}}$ are the global nodal force vector, global nodal displacement vector, and global stiffness matrix, respectively, expressed as

$$\mathbf{f}_{\mathrm{tot}} = \left(\mathbf{0}\ \mathbf{0}\ \ldots\ \mathbf{f}^{(N)}\right)^{\mathrm{T}} \tag{24}$$

$$\mathbf{p}_{\mathrm{tot}} = \left(\mathbf{p}^{(0)}\ \mathbf{p}^{(1)}\ \ldots\ \mathbf{p}^{(N)}\right)^{\mathrm{T}} \tag{25}$$

$$\mathbf{M}_{\mathrm{E,tot}} = \begin{bmatrix} \mathbf{M}_{\mathrm{E,LL}}^{(1)} & \mathbf{M}_{\mathrm{E,LR}}^{(1)} & \mathbf{0} & \mathbf{0} & \ldots & \mathbf{0} & \mathbf{0} \\ \mathbf{M}_{\mathrm{E,RL}}^{(1)} & \mathbf{M}_{\mathrm{E,RR}}^{(1)} + \mathbf{M}_{\mathrm{E,LL}}^{(2)} & \mathbf{M}_{\mathrm{LR}}^{(2)} & \mathbf{0} & \vdots & \vdots & \mathbf{0} \\ \mathbf{0} & \mathbf{M}_{\mathrm{E,RL}}^{(2)} & \mathbf{M}_{\mathrm{E,RR}}^{(2)} + \mathbf{M}_{\mathrm{E,LL}}^{(3)} & \ldots & \ldots & \vdots & \vdots \\ \mathbf{0} & \mathbf{0} & \vdots & \ddots & \vdots & \mathbf{0} & \mathbf{0} \\ \vdots & \ldots & \ldots & \mathbf{0} & \mathbf{M}_{\mathrm{E,RR}}^{(N-2)} + \mathbf{M}_{\mathrm{E,LL}}^{(N-1)} & \mathbf{M}_{\mathrm{E,LR}}^{(N-1)} & \mathbf{0} \\ \mathbf{0} & \ldots & \ddots & \mathbf{0} & \mathbf{M}_{\mathrm{E,RL}}^{(N-1)} & \mathbf{M}_{\mathrm{E,RR}}^{(N-1)} + \mathbf{M}_{\mathrm{E,LL}}^{(N)} & \mathbf{M}_{\mathrm{E,LR}}^{(N)} \\ \mathbf{0} & \mathbf{0} & \ldots & \mathbf{0} & \mathbf{0} & \mathbf{M}_{\mathrm{E,RL}}^{(N)} & \mathbf{M}_{\mathrm{E,RR}}^{(N)} \end{bmatrix} \tag{26}$$

in which superscript N denotes the N-th unit cell, and

$$\mathbf{f}^{(N)} = \left(0\ Q_{\mathrm{input}}\right)^{\mathrm{T}}, \quad \mathbf{p}^{(N)} = \left(w_{\mathrm{input}}\ \theta_{\mathrm{input}}\right)^{\mathrm{T}}, \quad \mathbf{p}^{(0)} = \left(w_{\mathrm{output}}\ \theta_{\mathrm{output}}\right)^{\mathrm{T}} \tag{27}$$

The transmission ratio is defined as [60]

$$\zeta = 20\log_{10}\left(\frac{\left|w_{\mathrm{output}}\right|}{\left|w_{\mathrm{input}}\right|}\right) \tag{28}$$

2.2 Timoshenko beam theory

To validate the result of the Euler–Bernoulli beam model, the dispersion relation using the Timoshenko beam model is also established. Different from Euler–Bernoulli beam theory, the Timoshenko beam theory considers rotary inertia and shear deformation, and hence, it is a higher order beam theory that allows beam modeling with considerable thickness [61]. The Timoshenko beam theory gives vibration governing equation as

$$\left(\mathrm{EI}+\frac{\mathrm{EIP}}{\kappa SG}\right)\frac{\mathrm{d}^4}{\mathrm{d}x^4}w\left(x\right)+\left(\frac{\mathrm{EI}\rho\omega^2}{\kappa G}+\rho I\omega^2+\frac{\rho IP\omega^2}{\kappa SG}-P\right)\frac{\mathrm{d}^2}{\mathrm{d}x^2}w\left(x\right)$$
$$+\left(\rho I\omega^2-\kappa SG\right)\frac{\rho\omega^2}{\kappa G}w\left(x\right)=0 \tag{29}$$

where κ is shear correction factor, G is shear modulus (Pa). The bending slope $\theta\left(x\right)$, bending moment $M\left(x\right)$, shear force $Q\left(x\right)$ are, respectively, expressed as

$$\theta\left(x\right)=R_1\left(\omega\right)\frac{\mathrm{d}}{\mathrm{d}x}w\left(x\right)+R_2\left(\omega\right)\frac{\mathrm{d}^3}{\mathrm{d}x^3}w\left(x\right) \tag{30}$$

$$M\left(x\right)=\mathrm{EI}\left[R_3\left(\omega\right)w\left(x\right)+R_4\frac{\mathrm{d}^2}{\mathrm{d}x^2}w\left(x\right)\right] \tag{31}$$

$$Q\left(x\right)=\kappa SG\left[1-R_1\left(\omega\right)\right]\frac{\mathrm{d}}{\mathrm{d}x}w\left(x\right)-\kappa SGR_2\left(\omega\right)\frac{\mathrm{d}^3}{\mathrm{d}x^3}w\left(x\right) \tag{32}$$

where $R_1\left(\omega\right)=\frac{\mathrm{EI}\rho S\omega^2+\kappa^2S^2G^2}{\kappa^2S^2G^2-\kappa SG\rho I\omega^2}$, $R_2\left(\omega\right)=\frac{\mathrm{EI}}{\kappa SG-\rho I\omega^2}+\frac{\mathrm{EIP}}{\kappa^2S^2G^2-\kappa SG\rho I\omega^2}$, $R_3\left(\omega\right)=-\rho\omega^2/\kappa G$, and $R_4=\left(-\kappa SG-P\right)/\kappa SG$.

The harmonic solution of Eq. (29) is assumed as $w\left(x\right)=A_\mathrm{T}e^{i\xi_\mathrm{T}x}$. Further substitution into Eq. (29), we have

$$B_1\xi_\mathrm{T}^4+B_2\xi_\mathrm{T}^2+B_3=0 \tag{33}$$

where

$$B_1=\mathrm{EI}+\frac{\mathrm{EIP}}{\kappa SG} \tag{34a}$$

$$B_2=P-\frac{\mathrm{EI}\rho\omega^2}{\kappa G}-\rho I\omega^2-\frac{\rho IP\omega^2}{\kappa SG} \tag{34b}$$

$$B_3=\left(\rho I\omega^2-\kappa SG\right)\frac{\rho\omega^2}{\kappa G} \tag{34c}$$

The roots to Eq. (33) are

$$\xi_{\mathrm{T},1}=-\xi_{\mathrm{T},2}=\sqrt{\frac{-B_2+\sqrt{B_2^2-4B_1B_3}}{2B_1}} \tag{35a}$$

$$\xi_{\mathrm{T},3}=-\xi_{\mathrm{T},4}=\sqrt{\frac{-B_2-\sqrt{B_2^2-4B_1B_3}}{2B_1}} \tag{35b}$$

Similarly, we can derive the relation between the nodal force vector $\mathbf{f}$ and nodal displacement vector $\mathbf{p}$ as

$$\begin{pmatrix}\mathbf{f}_1\\ \mathbf{f}_2\end{pmatrix}=\begin{bmatrix}\mathbf{M}_{\mathrm{T,LL}} & \mathbf{M}_{\mathrm{T,LR}}\\ \mathbf{M}_{\mathrm{T,RL}} & \mathbf{M}_{\mathrm{T,RR}}\end{bmatrix}\begin{pmatrix}\mathbf{p}_1\\ \mathbf{p}_2\end{pmatrix} \tag{36}$$

The dynamic stiffness matrix M_T can be expressed as

$$\mathbf{M}_\mathrm{T}=\begin{bmatrix}\mathbf{M}_{\mathrm{T,LL}} & \mathbf{M}_{\mathrm{T,LR}}\\ \mathbf{M}_{\mathrm{T,RL}} & \mathbf{M}_{\mathrm{T,RR}}\end{bmatrix}=\mathbf{V}_\mathrm{T}\mathbf{U}_\mathrm{T}^{-1} \tag{37}$$

where

$$\mathbf{U}_{\mathrm{T}} = \begin{bmatrix} 1 & 1 & 1 & 1 \\ \mathrm{iY}_1 & \mathrm{iY}_2 & \mathrm{iY}_3 & \mathrm{iY}_4 \\ e^{i\xi_{T,1}a} & e^{i\xi_{T,2}a} & e^{i\xi_{T,3}a} & e^{i\xi_{T,4}a} \\ \mathrm{iY}_1 e^{i\xi_{T,1}a} & \mathrm{iY}_2 e^{i\xi_{T,2}a} & \mathrm{iY}_3 e^{i\xi_{T,3}a} & \mathrm{iY}_4 e^{i\xi_{T,4}a} \end{bmatrix} \tag{38}$$

and

$$\mathbf{V}_{\mathrm{T}} = \begin{bmatrix} -Z_1 & -Z_2 & -Z_3 & -Z_4 \\ -\mathrm{iX}_1 & -\mathrm{iX}_2 & -\mathrm{iX}_3 & -\mathrm{iX}_4 \\ Z_1 e^{i\xi_{T,1}a} & Z_2 e^{i\xi_{T,2}a} & Z_3 e^{i\xi_{T,3}a} & Z_4 e^{i\xi_{T,4}a} \\ S_1 e^{i\xi_{T,1}a} & S_2 e^{i\xi_{T,2}a} & S_3 e^{i\xi_{T,3}a} & S_4 e^{i\xi_{T,4}a} \end{bmatrix} \tag{39}$$

The parameters Y_I,Z_I, X_I, and S_I with $I = 1, 2, 3, 4$ in Eqs. (38) and (39) are

$$Y_I = \xi_{T,I}\left(R_1 - R_2\xi_{T,I}^2\right) \tag{40a}$$

$$Z_I = \mathrm{EI}\left(R_3 - R_4\xi_{T,I}^2\right) \tag{40b}$$

$$X_I = \kappa SG\left(1 - R_1 + R_2\xi_{T,I}^2\right)\xi_{T,I} \tag{40c}$$

$$S_I = iX_I + D_{\mathrm{R}} \tag{40d}$$

Similar to Eqs. (17–28) in the prior section, we can first generalize a standard eigenvalue equation and then employ Eqs. (21–22) to solve the wavenumber k. Subsequently, the output and input displacements can be extracted from the global displacement vector by applying an input force and solving the global dynamic stiffness equation. The dispersion relation and transmission ratio of a Timoshenko beam can thus be determined.

3 Results and discussion

In this section, the dispersion relation and the transmission curve of this beam-resonator system will be studied analytically. Besides, the effects of axial tensile force, resonator number, and resonator mass will also be investigated systematically. For the sake of comparison with the results from Zhou et al. [54], the geometric parameters and material properties are taken as $b = 0.1$ m, $h = 0.002$ m, $a = 0.1$ m, $\rho = 2700$ kg/m^3, $E = 76.92$ GPa, $k_i = 9.593 \times 10^4$ N/m unless otherwise stated.

3.1 SDOF resonator

A comprehensive comparison is presented here to validate the theory and analytical solutions. For comparison purposes, the beam-resonator system is degenerated to a non-prestressed ($P = 0$) homogenous beam attached with an SDOF local resonator with $m_1 = 0.027$kg. The dispersion relation solved by Euler–Bernoulli beam theory and Timoshenko beam theory with that extracted from the referential study [54] are compared in Fig. 2. Here, the solid black line and blue star refer to the dispersion relation solved by the Euler beam theory and the Timoshenko beam theory, respectively, while red cycles refer to the result of Zhou et al. [54]. In Fig. 2a, the dispersion relation between angular frequency and the product of real part of wavenumber k and lattice constant a, denoted as ca, is presented. Comparatively, Fig. 2b indicates the attenuation coefficient as a function of ω. Generally, the attenuation coefficient is quantified by the product of imaginary part of wavenumber k and lattice constant, which is da [54]. Because it represents the evanescent Bloch wave, which decays least rapidly and carries energy farthest [62,63]. It can be observed that the results from the two beam theories are almost identical, and both agree excellently with the reference data either in real part or imaginary part. There are two bandgaps in Fig. 2a: the lower region marked by blue region from 243.5 to 362 Hz, and the higher region marked by gray region from 484.5 to 594.5 Hz. It is obvious that the bandgap ranges match perfectly with the nonzero part of attenuation coefficient in Fig. 2b. It confirms that flexural wave propagation can be efficiently prohibited in the bandgap range. By observing Fig. 2b, it is noticed that the higher part exhibits a gradual profile, while the lower part presents a sharp response, and the peak of the attenuation coefficient is much larger than that of the higher part. It is well known that BSBG generates a more gradual attenuation coefficient profile and the maximum value occurs in the middle of BSBG range. In contrast, the

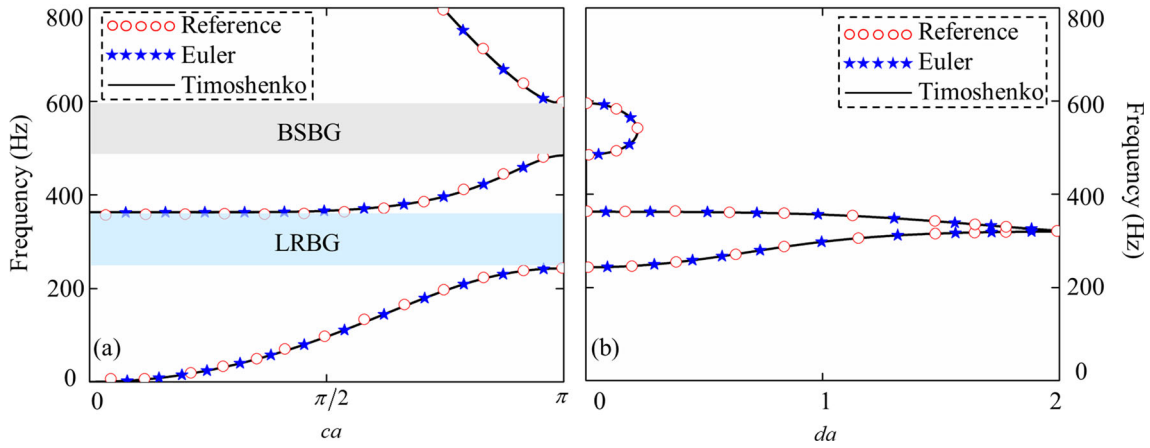

Fig. 2 Band structures of non-prestressed degenerated SDOF model. **a** Dispersion relation which is product of real part of the complex wavenumber and lattice constant. **b** Attenuation coefficient which is product of imaginary part of the complex wavenumber and lattice constant (color figure online)

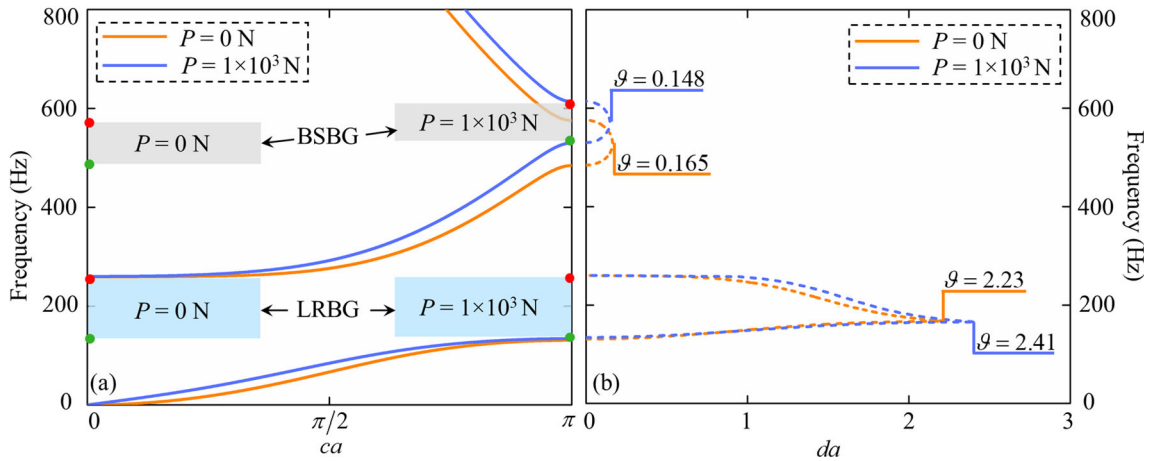

Fig. 3 Comparison of band structures of non-prestressed and prestressed SDOF models for **a** dispersion relation, and **b** attenuation coefficient (color figure online)

LRBG attenuation profile is antisymmetric and it shows a sharp response [49]. Such distinction has been commonly observed in the previous LR periodic systems [9,63–65]. Therefore, the lower bandgap and higher bandgap can be, respectively, regarded as LRBG and BSBG.

Since correctness of the theoretical derivation has been validated, and, for simplicity and practicability but without losing any generality, the resonator mass is adjusted from $m_1 = 0.027$ kg to $m_1 = 0.1$ kg. To better illustrate the influence of axial tensile force, an axial force $P = 1 \times 10^3$ N is applied along the OX direction and the dispersion relation is presented in the same figure with the non-prestressed ($P = 0$) condition, as shown in Fig. 3. The orange and blue solid lines in Fig. 3a are, respectively, the dispersion relations of $P = 0$ N and $P = 1 \times 10^3$ N, while the dashed lines in Fig. 3b correspond to the attenuation coefficient. The upper edge and lower edge of each bandgap are marked by a red and a green cycle, respectively. It is obvious the higher bandgap is more sensitive to axial force than lower bandgap. The natural frequency of the resonator, $\omega_r = \sqrt{k_1/m_1}/2\pi = 155.9$ Hz, is located in lower bandgap range, which again confirms the lower (higher) bandgap is LRBG (BSBG) [54]. To better explain the wave attenuation property, we further define a parameter ϑ to represent the maximum value of attenuation coefficient. It can be concluded from Fig. 3b that, unlike bandgap range, ϑ of LRBG is more sensitive than BSBG. For example, by increasing P from 0 N to 1×10^3 N, ϑ of LRBG increases by 0.18, while ϑ of BSBG decreases by 0.017. Besides, LRBG has larger ϑ than BSBG which means it can perform better than BSBG in wave attenuation.

Having presented some specific cases of analysis, a general parametric study on axial force is presented to investigate the effect of axial force more comprehensively. As presented in Fig. 4, by increasing the axial

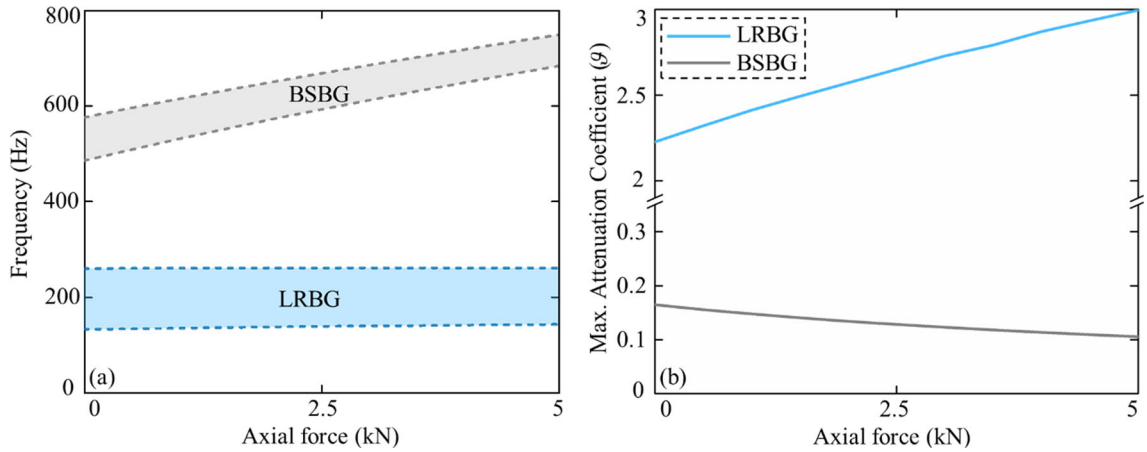

Fig. 4 Tunable **a** bandgap and **b** maximum attenuation coefficient ϑ with respect to axial tensile force P

force from 0 N to 5 kN, the upper band and lower band of BSBG at $ca = \pi$ both increase, but BSBG becomes narrower. For example, the width of BSBG for $P = 0$ N is 90 Hz (485–575 Hz) while it becomes 66 Hz (683–749 Hz) when $P = 5$ kN. By contrast, axial force only shows minor influence on LRBG; for example, the lower edge raises by 10 Hz (132–142 Hz) and the upper edge only increases by 1 Hz (259–260 Hz). From Fig. 4b, we notice the maximum attenuation coefficient ϑ of LRBG is obviously increased with increasing P while ϑ of BSBG decreases slightly, which is identical to the phenomenon in Fig. 3b. Therefore, axial force can be utilized to increase ϑ of LRBG and to tune the frequency range of BSBG with only a slight reduction on the maximum attenuation coefficient ϑ. However, the LRBG range is insensitive to axial force.

3.2 MDOF resonator

Based on the previous discussion, we know that the proposed beam system possesses one BSBG and one LRBG when it is attached with SDOF resonators. For a better understanding of the dependence of bandgaps on resonator number, the characteristic of beam attached with MDOF resonator is studied in this section. Here, we mainly focus on the effect of resonator number on bandgap width and LRBG number. Similar to the previous analysis, n and i represent the number of resonators and the i-th resonator, respectively, and the response of $n = 2, 3, 4$ is studied herein. For comparison, the resonator mass and spring stiffness remain identical to the previous analysis, which are $m_i = 0.1$ kg and $k_i = 9.593 \times 10^4$ N/m. From Eqs. (21) and (22), the dispersion relation of a non-prestressed homogenous beam attached with MDOF resonators can be determined. In Fig. 5a–f, the dispersion relation and attenuation coefficient for $n = 2, 3, 4$, respectively, are presented. The black line and blue stars denote, respectively, the solutions of Timoshenko beam theory and Euler–Bernoulli beam theory. The blue, green, orange, and pink regions, which are marked by Roman numerals I, II, III, IV, respectively, represent the u-th ($u = 1, 2, 3, 4$) LRBG. It is noticeable that adding a resonator can generate a new bandgap and the resonator number is always identical to the LRBG number while there is always one BSBG no matter how many resonators are attached. In addition, the location and width of BSBG and ϑ for each bandgap remain almost unchanged. For example, the width of BSBG only increases from 90.75 Hz to 91.5 Hz by changing $n = 2$ to $n = 4$. However, the influence of resonator number on total LRBG width cannot be directly perceived from Fig. 5.

To investigate the influence of resonator number n more comprehensively, a parameter study on n is conducted. The remaining resonator masses and spring stiffnesses are $m_i = 0.1$ kg and $k_i = 9.593 \times 10^4$ N/m, respectively. As presented in Fig. 6, the resonator number increases from $n = 1$ to $n = 15$, and we focus on the total bandgap width (blue dash line), total LRBG width (red dash line), and starting point of BG (orange solid line). It is observed that both total BG width and total LRBG width do obviously increase by having more resonators. For example, the total BG width is enhanced from 219.75 Hz to 263.75 Hz by increasing n from $n = 1$ to $n = 15$. However, the difference between total BG width and total LRBG width (shadow area) is almost constant, which means the BSBG width only changes slightly. For instance, the BSBG width is 90.75 Hz when there is one resonator, and it increases by 1.38% to 92 Hz when there are 15 resonators. Therefore, it is LRBG that mainly contributes to the increase in the total bandgap width. On the other hand,

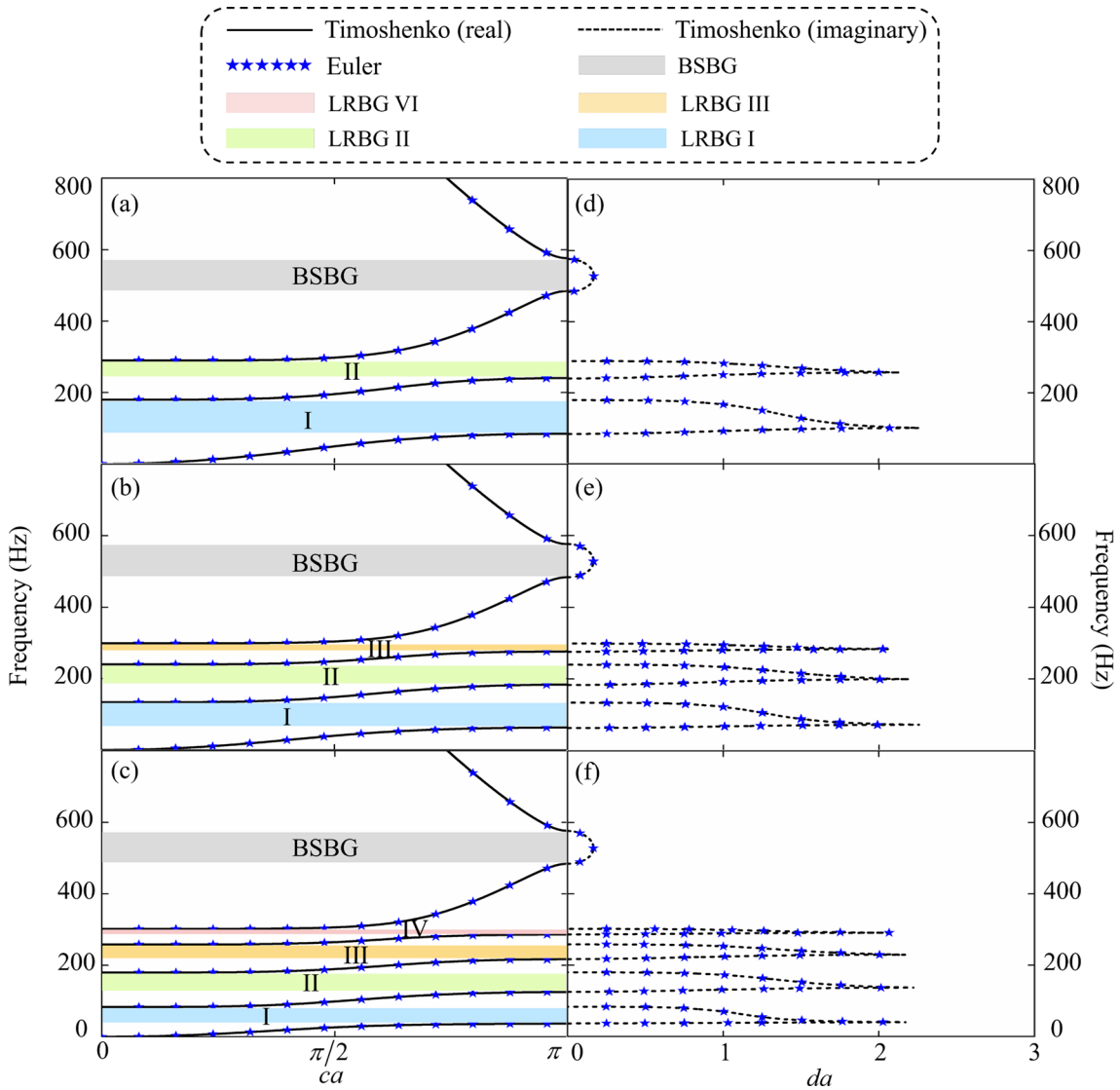

Fig. 5 Dispersion relation of LR beam attached with **a** 2 resonators, **b** 3 resonators, **c** 4 resonators; and the corresponding attenuation coefficient with **d** 2 resonators; **e** 3 resonators **f** 4 resonators. The resonator mass is $m_i = 0.1$ kg (color figure online)

it is noticed that the starting point of BG decreases dramatically with increasing n. For example, the starting point of BG decreases by 93.3% with the increase of n from 1 to 15. Therefore, adding more resonators can help generate low frequency bandgaps. Some potential applications in AMs can be established based on this low frequency bandgap generation mechanism. Besides, we can observe marginal effect with increasing n, regardless it is the total BG width, total LRBG width or starting point of BG. The increase (decrease) in the total LRBG width (starting point of BG) after adding one resonator becomes less when n becomes larger. For example, the starting point of BG decreases by 116.5 Hz (131 Hz−14.5 Hz) with n increasing from $n = 1$ to $n = 8$, while it only decreases by 5.75 Hz (14.5 Hz−8.75 Hz) when n is further increased from $n = 8$ to $n = 15$. This finding suggests a more economical method for further potential applications about generating low-frequency bandgap or enlarging bandgap width.

The foregoing discussion concludes that additional resonators cause an increase in the total LRBG width and generation of low frequency bandgap. However, adding resonators change the total resonator number and mass simultaneously. It is still not clear whether the change is due to the resonator number or resonator mass. Therefore, two parametric studies are conducted here for this purpose.

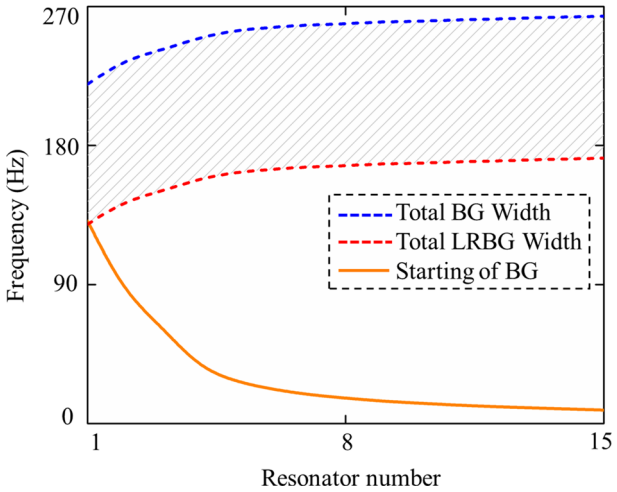

Fig. 6 Tunable bandgap width and starting frequency of BG by adding more resonators (color figure online)

Table 1 Details of resonator mass and bandgap for Cases 1, 2, 3

Case	Resonator mass (kg)			Total LRBG (Hz)	BSBG (Hz)	Total BG (Hz)	Start of BG (Hz)
	m_1	m_2	m_3				
1	0.6	0	0	165	86.25	251.25	53.75
2	0.2	0.4	0	162.5	89	251.5	46
3	0.1	0.2	0.3	160.5	91.5	252	40.5

In the first study, the total resonator mass is maintained as $\sum m_i = 0.6$ kg and the resonator number increases from $n = 1$ to $n = 3$. As shown in Table 1, $n = 1, 2, 3$ refer to Cases 1,2,3, respectively, and the details are presented in Table 1. In Case 1, only one resonator is attached and the mass is $m_1 = 0.6$ kg. Then, one more resonator is added and the total mass is kept unchanged, Case 2 thus, becomes $m_1 = 0.2$ kg, $m_2 = 0.4$ kg. Similarly, Case 3 is $m_1 = 0.1$ kg, $m_2 = 0.2$ kg, $m_3 = 0.3$ kg. From Eq. (23), the dispersion relations of these three cases are solved and presented in Fig. 7. Here, Fig. 7a–c correspond to Cases 1–3 in Table 1, respectively. The phenomenon analogous to Fig. 5 can be observed. Whenever an additional resonator is introduced, a new LRBG occurs. Besides, it is noticeable the starting point of LRBG becomes lower, while accurate bandgap width cannot be perceived from Fig. 7 directly. For more accurate analysis of the influence of n on band structure, the relevant datas on bandgaps are presented in Table 1. Identical to the phenomenon in Figs. 5 and 6, the starting point of bandgap becomes lower. However, the degree of influence is obviously smaller. For example, the starting point of BG in Fig. 6 decreases by 51.9% (131 Hz−63 Hz) by increasing resonator number from $n = 1$ to $n = 3$, while it only decreases by 25.6% (53.75 Hz−40.5 Hz) in Fig. 7. It can be observed in Table 1 that the BSBG width increases by increasing resonator number while retaining the total mass. Interestingly, the total LRBG width decreases and thus, reduces the increase in total BG width such that the total BG width is kept at a relevant stable level. However, it is still not conclusive whether it is not the resonator number that increases the total bandgap width. The other control variable study is thus necessary.

The second parametric study is related to the effect of increasing the total resonator mass while keeping the resonator number unchanged as $n = 2$. Three different cases are considered with the details shown in Table 2. In Case 4, the resonator masses are $m_1 = 0.1$ kg and $m_2 = 0.2$ kg. The resonator masses in Case 5 and Case 6 are obtained by doubling and tripling the corresponding resonator masses in Case 1, respectively. The bandgap width solutions are listed in Table 2, and the dispersion relations are plotted in Fig. 8, where Fig. 8a–c correspond to Cases 4–6, respectively. It can be observed the BSBG width becomes a little smaller, while the location almost keeps in the same range. We also notice both LRBG I and LRBG II move forward to a lower frequency range. However, the width of LRBG I and LRBG II show an inverse trend: LRBG II becomes wider while LRBG I becomes narrower. For example, the width of LRBG I (LRBG II) decreases (increases) from 85.75 Hz (62.75 Hz) in Case 4 to 65.25 Hz (102.5 Hz) in Case 6. As seen in Table 2, because of the dramatic increase in total LRBG width, the total BG width can still be further enlarged by increasing total resonator mass although the BSBG width is slightly decreased. In addition, the starting point of BG becomes smaller,

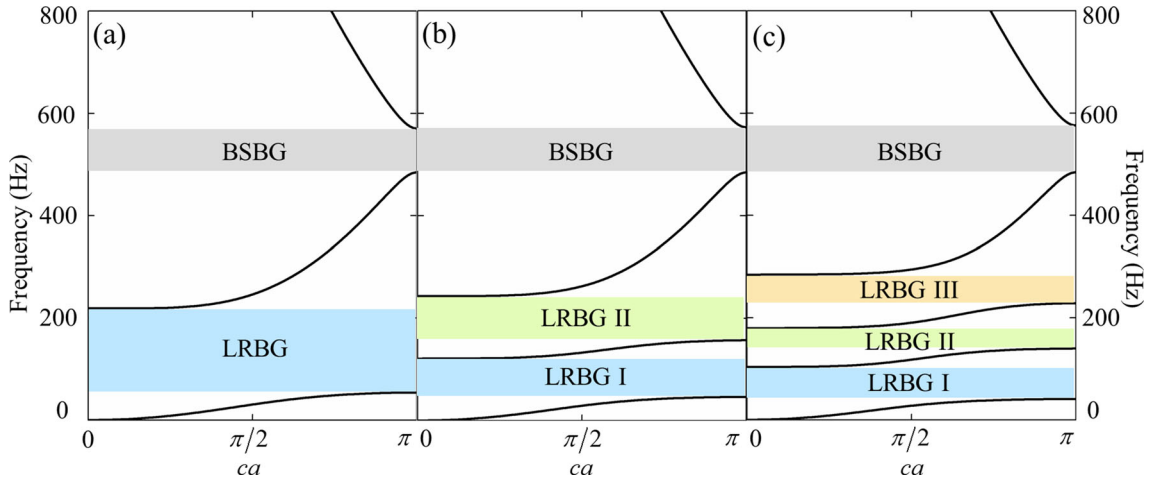

Fig. 7 Dispersion relation of LR beam attached with **a** 1 resonator, **b** 2 resonators, **c** 3 resonators while retaining the total resonator mass

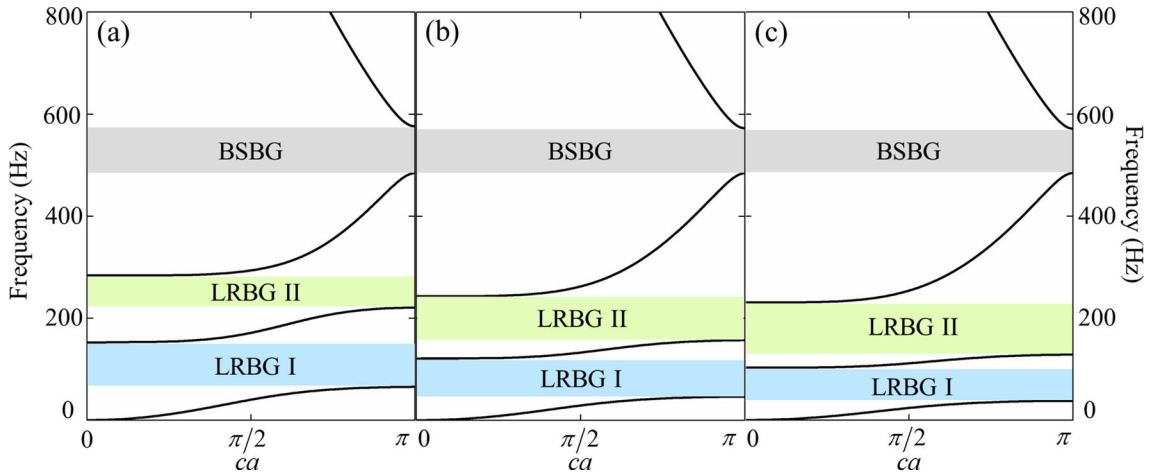

Fig. 8 Dispersion relation of LR beam attached with 2 resonators with total resonator mass is **a** 0.3 kg **b** 0.6 kg, **c** 0.9 kg

Table 2 Details of resonator mass and bandgap for Cases 4, 5, 6

Case	Resonator mass (kg)		LRBG I (Hz)	LRBG II (Hz)	Total LRBG (Hz)	BSBG (Hz)	Total BG (Hz)	Start of BG (Hz)
	m_1	m_2						
4	0.1	0.2	85.75	62.75	148.5	91.25	239.75	65.5
5	0.2	0.4	74.75	86.5	161.25	88	249.25	46.25
6	0.3	0.6	65.25	102.5	167.75	86.75	254.5	37.75

which is identical to the phenomenon discussed above. Based on Figs. 7 and 8 and Tables 1 and 2, we may conclude the increasing resonator number and mass can generate a lower frequency bandgap. However, it is the total resonator mass that really influences the total LRBG width. Further, neither the resonator number nor the resonator mass can greatly affect the BSBG location and width.

The analysis above shows that changing n while keeping the total mass constant does not induce any significant effect on the total bandgap width. In the analysis above, however, the resonators mass is incremental with their distance to the beam, i.e., $m_i < m_{i+1}$. The effect of resonator mass distribution on the LRBGs width and location is not clear. In the following analysis, the total resonator number and mass will be kept constant while the distribution of the resonator mass will be arranged in different ways. As shown in Table 3, the total resonator mass is retained as $\sum m_i = 0.6$ kg and three different cases, Cases 7–9, are considered In Case 7, the resonators mass are $m_1 = 0.2$ kg and $m_2 = 0.4$ kg; the mass is equally distributed in Case 8 as $m_1 = m_2 = 0.3$

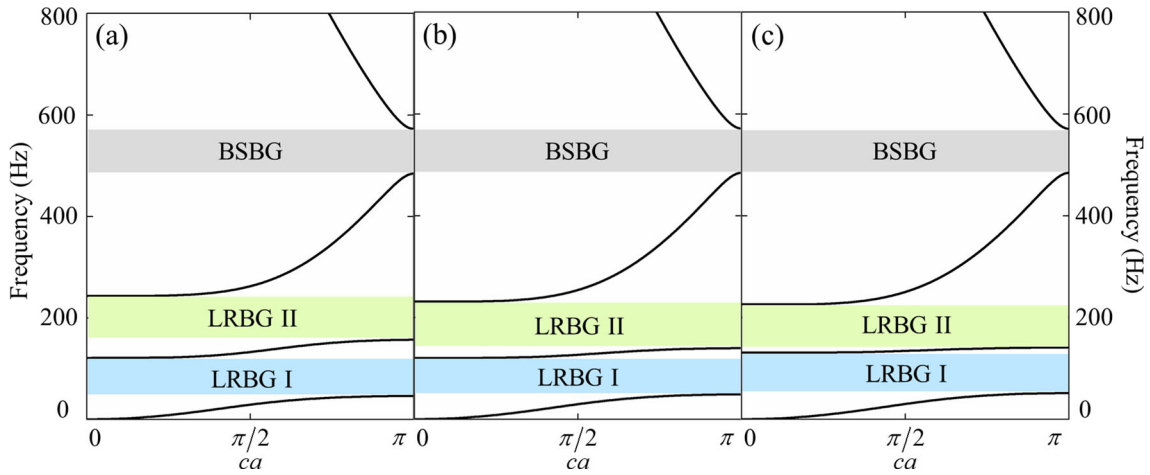

Fig. 9 Dispersion relation of LR beam attached with 2 resonators with the total resonator mass 0.6 kg, for **a** $m_1 < m_2$, **b** $m_1 = m_2$, **c** $m_1 > m_2$

Table 3 Detail resonator mass and bandgap condition of Cases 7, 8, 9

Case	Resonator mass (kg)		LRBG I (Hz)	LRBG II (Hz)	Total LRBG (Hz)	BSBG (Hz)	Total BG (Hz)	Start of BG (Hz)
	m_1	m_2						
7	0.2	0.4	74.75	86.5	161.25	88	249.25	46.25
8	0.3	0.3	71.5	91.75	163.25	86.75	250	49
9	0.4	0.2	79.25	84.5	163.75	86.5	250.25	51.75

kg; while m_1 (m_2) is adjusted to $m_1 = 0.4$ kg ($m_2 = 0.2$ kg) in Case 9. The dispersion relations for Cases 7-9 are presented in Fig. 9a–c. It is observed that LRBG I moves forward to a higher frequency range while LRBG II steps to a lower frequency range, i.e., the gap between LRBG II and LRBG I becomes narrower. For instance, in Case 7, LRBG I ends at 121 Hz and LRBG II starts at 157 Hz, the gap is 36 Hz. In Case 9, the gap between LRBG I and LRBG II becomes 10.25 Hz (131 Hz−141.25 Hz). The bandgaps width for each case is listed in Table 3. It is observed that LRBG I becomes narrower while LRBG II becomes wider with an equal distribution of resonator mass. However, mass distribution only influences slightly on the total LRBG width.

3.3 Actively control of bandgap

As mentioned in the previous section, the spring stiffness k_i is tunable via tuning the active stiffness $k_{i,a}$. To study the effect of spring stiffness, the dispersion relation for $k_1 = k_2 = 6 \times 10^4$ and $k_1 = k_2 = 9 \times 10^4$ N for $m_1 = 0.2$ kg, $m_2 = 0.4$ kg is presented. The result is shown in Fig. 10a where the red solid line refers to $k_{1,2} = 9 \times 10^4$ N while the blue dash line is that of $k_{1,2} = 6 \times 10^4$ N. It is observed that increasing spring stiffness raises LRBG I and LRBG II and the bandgap width is also slightly increased. For example, the width of LRBG I for $k_{1,2} = 6 \times 10^4$ N is 58 Hz (38–96 Hz), while that of $k_{1,2} = 9 \times 10^4$ N is increased by 14.7% to 66.5 Hz (45 Hz−111.5 Hz). Besides, BSBG is broadened with the upper boundary increasing while the lower boundary keeping unchanged at 484.5 Hz.

For the sake of a more comprehensive investigation, a parametric study on spring stiffness is conducted. As shown in Fig. 10b, a bandgap map is presented for a range of stiffness from 2×10^4 N to 10×10^4 N. As concluded in Fig. 10, the bandgaps can be broadened and raised except for the lower boundary of BSBG which is almost constant. In this case, LRBG I, LRBG II, and BSBG are, respectively, enlarged by 135.1%, 136%, and 369.2% by tuning the spring stiffness from 2×10^4 N to 10×10^4 N.

The previous analysis indicates that the bandgap range and width are affected by both resonator mass and spring stiffness. We further analyze the combined effect of resonator mass and spring stiffness by defining $m_1 = m_2$, $k_1 = k_2$ and sweeping $m_{1,2}$ from 0.1 kg to 1 kg and $k_{1,2}$ from 2×10^4 N to 10×10^4 N. In Fig. 11a–c, the effect on LRBG I, LRBG II, and BSBG is presented, respectively, where purple refers to the lower frequency range while dark red denotes the higher frequency range. For either LRBG I or LRBG II, it

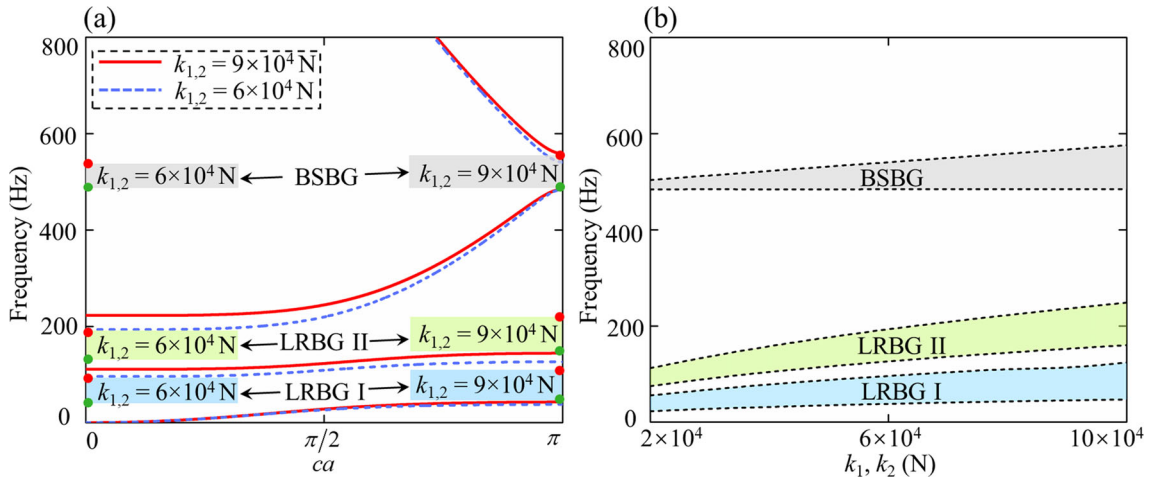

Fig. 10 **a** Dispersion relation for $k_1 = k_2 = 6 \times 10^4$, $k_1 = k_2 = 9 \times 10^4$, with $m_1 = 0.2$ kg, $m_2 = 0.4$ kg, and **b** a parametric study for k_1, k_2, with $k_1 = k_2$, $m_1 = 0.2$ kg, $m_2 = 0.4$ kg (color figure online)

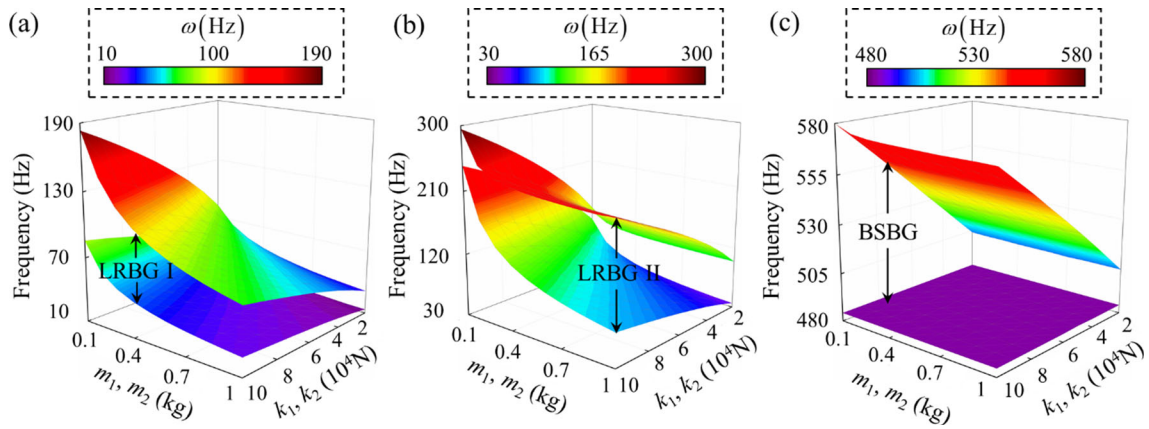

Fig. 11 The bandgap map for **a** LRBG I, **b** LRBG II, **c** BSBG for different resonator masses and spring stiffness with $k_1 = k_2$ and $m_1 = m_2$ (color figure online)

is observed that increasing spring stiffness enlarges the bandgap width while lowering resonator mass causes the generation of higher frequency bandgap. On the other hand, LRBG I becomes narrower with increasing resonator mass while the behavior of LRBG II is opposite. Taking $k_1 = k_2 = 8 \times 10^4$ N as an example, the LRBG I width decreases by 47.5% (85.5–38 Hz) via increasing resonator number $m_{1,2}$ from 0.1 kg to 1 kg, but LRBG II increases by 188.6% (44–127 Hz). From Fig. 11c, it is easily noticed that the upper boundary of BSBG is sensitive to spring stiffness and can be slightly influenced by resonator mass. For the lower boundary, however, it is independent of both resonator mass and spring stiffness.

Having discussed the proposed band structure, and the effects of axial force, resonator mass, and spring stiffness on band structure, we now turn to analyze the flexural wave propagation behavior. As stated above, flexural wave propagation in a bandgap could be weakened or prohibited, and this is known as wave attenuation. To analyze this wave propagation behavior, we first construct a supercell model by arranging 20 unit cells in the OX direction. An external excitation force is applied at the right end and the input (output) displacement is detected at the right (left) end. Using Eq. (28), we herein quantify wave propagation by introducing a transmission ratio, as shown in Fig. 12. For the sake of comparison and universality, the unit cells used in Fig. 12a–c correspond to the cases in Fig. 5a–c, respectively. The colored shadow area is the unit cell bandgap range. It can be observed that the transmission ratio is obviously and significantly decreased in the bandgap range of unit-cell, which implies that flexural wave propagation can be effectively prohibited. Besides, the wave attenuation range matches perfectly with the unit cell bandgap range.

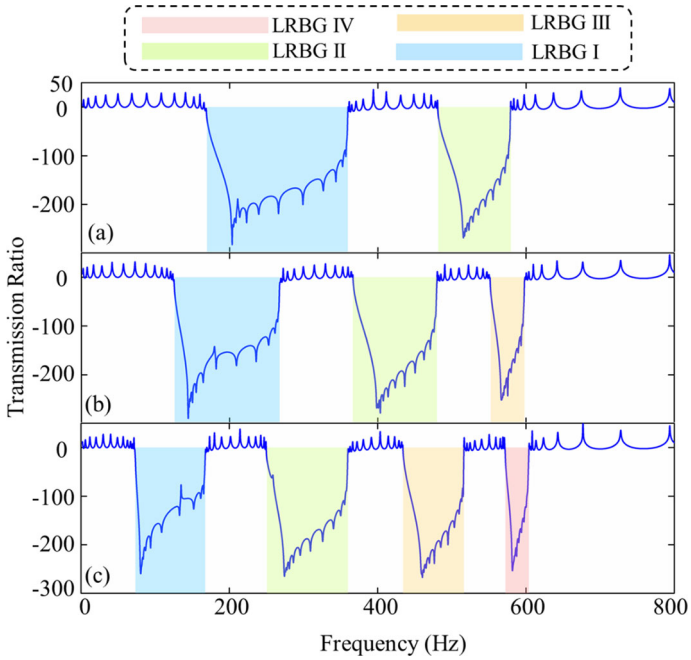

Fig. 12 Transmission ratio of LR beam attached with **a** 2 resonators, **b** 3 resonators, **c** 4 resonators. The resonator masses are identical, where $m_i = 0.1$ kg (color figure online)

4 Conclusion

In this paper, a comprehensive investigation on the theory, modeling, and numerical analysis for a metamaterial beam system that comprises an extensible homogenous beam, with actively controllable piezoelectric springs and MDOF local resonators, is established. The Euler–Bernoulli beam theory and Timoshenko beam theory are applied to derive the governing equation of motion. The analytical dispersion relation is obtained by SEM, and a comparison with reference to benchmark data is presented to verify the accuracy and validity of the theory and models. The band structure indicates the presence of BSBG and LRBG for the beam system. The influence of axial force, resonator number, total resonator mass, and resonator mass distribution are fully analyzed. It is concluded from the study that an axial tensile force can significantly raise the BSBG frequency range; however, the bandgap width becomes narrow simultaneously. Comparatively, the axial force only slightly affects the range and width of LRBG while the attenuation coefficient of LRBG is sensitive to the axial force. Further, resonators can be exploited to tune LRBG, frequency range, and distance between LRBG. It is observed that LRBG is always identical to the local resonator number. From a parametric study, it is concluded that adding the total resonator mass or number can help generate a lower frequency bandgap while only a larger total resonator mass can produce a wider LRBG. On the other hand, the gap between LRBGs becomes narrow when the resonator masses decrease away from the beam, i.e., $m_i > m_{i+1}$. Active control of bandgap can be established by tuning the piezoelectric spring stiffness. Both LRBG and BSBG are found to be broadened by increasing spring stiffness. Therefore, techniques for passive control (changing resonator mass) and active control (tuning piezoelectric spring stiffness) can be achieved by ways of introducing local resonators and piezoelectric spring. Hence, the application potential of metamaterial beam systems can be greatly enhanced with effective control techniques. In addition, the wave attenuation performance can be quantified by analyzing the transmission ratio. In this regard, the flexural wave propagation is found to be obviously prohibited in the bandgap range. In general, this present study has established a comprehensive investigation for the effects of axial force and resonators on band structure and flexural wave propagation. New passive and active control techniques of dispersive wave characteristics introduced here provide distinct insights for future engineering applications.

Acknowledgements The work described in this paper was supported by National Natural Science Foundation of China through a research grant awarded to the City University of Hong Kong Shenzhen Research Institute (Project No. 12072165).

References

1. Yuan, L., Cai, Z., Zhao, P., Ding, Y., Ma, T., Wang, J.: Flexural wave propagation in periodic tunnels with elastic foundations. Mech. Adv. Mater. Struct. (2020). https://doi.org/10.1080/15376494.2020.1769233
2. Zou, C., Wang, Y., Wang, P., Guo, J.: Measurement of ground and nearby building vibration and noise induced by trains in a metro depot. Sci. Total Environ. **536**, 761–773 (2015). https://doi.org/10.1016/j.scitotenv.2015.07.123
3. Vogiatzis, K., Mouzakis, H.: Ground-borne noise and vibration transmitted from subway networks to multi-storey reinforced concrete buildings. Transport **33**, 446–453 (2018). https://doi.org/10.3846/16484142.2017.1347895
4. Sun, X., Yuan, Y., Ma, M., Liu, W.: Prediction of metro train-induced low frequency vibration responses in far field. J. Vib. Shock. **36**, 198–202 (2017). https://doi.org/10.13465/j.cnki.jvs.2017.04.031
5. Hong, J., He, Z., Zhang, G., Mi, C.: Tunable Bandgaps in Phononic Crystal Microbeams Based on Microstructure. Piezo Temp. Eff. Cryst. **11**, 1029 (2021). https://doi.org/10.3390/cryst11091029
6. Lee, T., Iizuka, H.: Bragg scattering based acoustic topological transition controlled by local resonance. Phys. Rev. B. (2019). https://doi.org/10.1103/PhysRevB.99.064305
7. Narayanamurti, V., Störmer, H., Chin, M., Gossard, A., Wiegmann, W.: Selective transmission of high-frequency phonons by a superlattice: the "dielectric" phonon filter. Phys. Rev. Lett. **43**, 2012 (1979). https://doi.org/10.1103/PhysRevLett.43.2012
8. Guo, X., Ji, S., Liu, H., Ren, K.: Dispersion relations of elastic waves in three-dimensional cubical piezoelectric phononic crystal with initial stresses and mechanically and dielectrically imperfect interfaces. Appl. Math. Model. **69**, 405–424 (2019). https://doi.org/10.1016/j.apm.2018.12.023
9. Liu, Z., Zhang, X., Mao, Y., Zhu, Y., Yang, Z., Chan, C.T., Sheng, P.: Locally resonant sonic materials. Science **289**, 1734–1736 (2000). https://doi.org/10.1126/science.289.5485.1734
10. Li, J., Chan, C.T.: Double-negative acoustic metamaterial. Phys. Rev. E **70**, 055602 (2004). https://doi.org/10.1103/PhysRevE.70.055602
11. Zhang, X., Liu, Z.: Negative refraction of acoustic waves in two-dimensional phononic crystals. Appl. Phys. Lett. **85**, 341–343 (2004). https://doi.org/10.1063/1.1772854
12. Brunet, T., Merlin, A., Mascaro, B., Zimny, K., Leng, J., Poncelet, O., Aristégui, C., Mondain-Monval, O.: Soft 3D acoustic metamaterial with negative index. Nat. Mater. **14**, 384–388 (2015). https://doi.org/10.1038/nmat4164
13. Mitchell, S.J., Pandolfi, A., Ortiz, M.: Effect of brittle fracture in a metaconcrete slab under shock loading. J. Eng. Mech. **142**, 04016010 (2016). https://doi.org/10.1061/(ASCE)EM.1943-7889.0001034
14. Fang, N., Xi, D., Xu, J., Ambati, M., Srituravanich, W., Sun, C., Zhang, X.: Ultrasonic metamaterials with negative modulus. Nat. Mater. **5**, 452–456 (2006). https://doi.org/10.1038/nmat1644
15. Ding, Y., Liu, Z., Qiu, C., Shi, J.: Metamaterial with simultaneously negative bulk modulus and mass density. Phys. Rev. Lett. **99**, 093904 (2007). https://doi.org/10.1103/PhysRevLett.99.093904
16. Cai, C., Zhou, J., Wu, L., Wang, K., Xu, D., Ouyang, H.: Design and numerical validation of quasi-zero-stiffness metamaterials for very low-frequency band gaps. Compos. Struct. **236**, 111862 (2020). https://doi.org/10.1016/j.compstruct.2020.111862
17. Zhou, J., Pan, H., Cai, C., Xu, D.: Tunable ultralow frequency wave attenuations in one-dimensional quasi-zero-stiffness metamaterial. Int. J. Mech. Mater. Des. **17**, 285–300 (2021). https://doi.org/10.1007/s10999-020-09525-7
18. Vasseur, J.O., Hladky-Hennion, A.-C., Djafari-Rouhani, B., Duval, F., Dubus, B., Pennec, Y., Deymier, P.: Waveguiding in two-dimensional piezoelectric phononic crystal plates. J. Appl. Phys. **101**, 114904 (2007). https://doi.org/10.1063/1.2740352
19. Liu, G.-S., Zhou, Y., Liu, M.-H., Yuan, Y., Zou, X.-Y., Cheng, J.-C.: Acoustic waveguide with virtual soft boundary based on metamaterials. Sci. Rep. **10**, 1–7 (2020). https://doi.org/10.1038/s41598-020-57986-9
20. Chen, Z., Zhou, W., Lim, C.W.: Tunable frequency response of topologically protected interface modes for membrane-type metamaterials via voltage control. J. Sound Vibr. **494**, 115870 (2021). https://doi.org/10.1016/j.jsv.2020.115870
21. Chang, I.-L., Liang, Z.-X., Kao, H.-W., Chang, S.-H., Yang, C.-Y.: The wave attenuation mechanism of the periodic local resonant metamaterial. J. Sound Vibr. **412**, 349–359 (2018). https://doi.org/10.1016/j.jsv.2017.10.008
22. Sumbatyan, M., Remizov, M.: On 3D theory of acoustic metamaterials with a triple-periodic system of interior obstacles. Contin. Mech. Thermodyn. **31**, 1743–1756 (2019). https://doi.org/10.1007/s00161-019-00745-7
23. Nguyen, H., Wu, Q., Chen, H., Chen, J., Yu, Y., Tracy, S., Huang, G.: A Fano-based acoustic metamaterial for ultra-broadband sound barriers. Proc. R. Soc. A. **477**, 20210024 (2021). https://doi.org/10.1098/rspa.2021.0024
24. Pai, P.F., Peng, H., Jiang, S.: Acoustic metamaterial beams based on multi-frequency vibration absorbers. Int. J. Mech. Sci. **79**, 195–205 (2014). https://doi.org/10.1016/j.ijmecsci.2013.12.013
25. Liang, Z., Li, J.: Extreme acoustic metamaterial by coiling up space. Phys. Rev. Lett. **108**, 114301 (2012). https://doi.org/10.1103/PhysRevLett.108.114301
26. Madeo, A., Neff, P., Ghiba, I.-D., Placidi, L., Rosi, G.: Wave propagation in relaxed micromorphic continua: modeling metamaterials with frequency band-gaps. Contin. Mech. Thermodyn. **27**, 551–570 (2015). https://doi.org/10.1007/s00161-013-0329-2
27. Dertimanis, V.K., Antoniadis, I.A., Chatzi, E.N.: Feasibility analysis on the attenuation of strong ground motions using finite periodic lattices of mass-in-mass barriers. J. Eng. Mech. **142**, 04016060 (2016). https://doi.org/10.1061/(ASCE)EM.1943-7889.0001120
28. Fok, L., Ambati, M., Zhang, X.: Acoustic metamaterials. MRS Bull. **33**, 931–934 (2008). https://doi.org/10.1557/mrs2008.202
29. Chen, Z., Wang, G., Zhou, W., Lim, C.W.: Elastic foundation induced wide bandgaps for actively-tuned topologically protected wave propagation in phononic crystal beams. Int. J. Mech. Sci. **194**, 106215 (2021). https://doi.org/10.1016/j.ijmecsci.2020.106215
30. Chen, Z., Wang, G., Lim, C.W.: Periodically alternated elastic support induced topological phase transition in phononic crystal beam systems. Int. J. Solids Struct. **239**, 111461 (2022). https://doi.org/10.1016/j.ijsolstr.2022.111461
31. Li, Y., Chen, T., Wang, X., Xi, Y., Liang, Q.: Enlargement of locally resonant sonic band gap by using composite plate-type acoustic metamaterial. Phys. Lett. A **379**, 412–416 (2015). https://doi.org/10.1016/j.physleta.2014.11.028

32. Ding, C., Hao, L., Zhao, X.: Two-dimensional acoustic metamaterial with negative modulus. J. Appl. Phys. **108**, 074911 (2010). https://doi.org/10.1063/1.3493155
33. Chen, Z., Muhammad, Wang, X., Lim, C.W.: Low frequency topologically protected wave transport in sinusoidal lightweight acoustic metamaterials. J. Appl. Phys. 130, 045108 (2021). https://doi.org/10.1063/5.0050963
34. Chen, Z., Lim, C.W., Shi, F.: A review on seismic metamaterials: From natural toartificial structures. Chin. Sci. Bull. (2021). https://doi.org/10.1360/TB-2021-0517
35. Wen, S., Xiong, Y., Hao, S., Li, F., Zhang, C.: Enhanced band-gap properties of an acoustic metamaterial beam with periodically variable cross-sections. Int. J. Mech. Sci. **166**, 105229 (2020). https://doi.org/10.1016/j.ijmecsci.2019.105229
36. Jia, Z., Chen, Y., Yang, H., Wang, L.: Designing phononic crystals with wide and robust band gaps. Phys. Rev. Appl. **9**, 044021 (2018). https://doi.org/10.1103/PhysRevApplied.9.044021
37. Jiang, S., Chen, H., Dai, L., Hu, H., Laude, V.: Multiple low-frequency broad band gaps generated by a phononic crystal of periodic circular cavity sandwich plates. Compos. Struct. **176**, 294–303 (2017). https://doi.org/10.1016/j.compstruct.2017.05.048
38. Wang, G., Wen, J., Wen, X.: Quasi-one-dimensional phononic crystals studied using the improved lumped-mass method: Application to locally resonant beams with flexural wave band gap. Phys. Rev. B **71**, 104302 (2005). https://doi.org/10.1103/PhysRevB.71.104302
39. Liu, Y., Yu, D., Li, L., Zhao, H., Wen, J., Wen, X.: Design guidelines for flexural wave attenuation of slender beams with local resonators. Phys. Lett. A **362**, 344–347 (2007). https://doi.org/10.1016/j.physleta.2006.10.056
40. Bao, H., Wu, C., Wang, K., Yan, B.: An enhanced dual-resonator metamaterial beam for low-frequency vibration suppression. J. Appl. Phys. (2021). https://doi.org/10.1063/5.0040414
41. Wang, X., Wang, M.Y.: An analysis of flexural wave band gaps of locally resonant beams with continuum beam resonators. Meccanica **51**, 171–178 (2016). https://doi.org/10.1007/s11012-015-0197-x
42. Lu, K., Wu, J.H., Jing, L., Guan, D.: Flexural vibration bandgaps in local resonance beam with a novel two-degree-of-freedom local resonance system. Eur. Phys. J. Appl. Phys. **77**, 20501 (2017). https://doi.org/10.1051/epjap/2017160410
43. Wu, K., Hu, H., Wang, L.: Optimization of a type of elastic metamaterial for broadband wave suppression. Proc. R. Soc. A. **477**, 20210337 (2021). https://doi.org/10.1098/rspa.2021.0337
44. Casalotti, A., El-Borgi, S., Lacarbonara, W.: Metamaterial beam with embedded nonlinear vibration absorbers. Int. J. Non-Linear Mech. **98**, 32–42 (2018). https://doi.org/10.1016/j.ijnonlinmec.2017.10.002
45. Hu, G., Tang, L., Cui, X.: On the modelling of membrane-coupled Helmholtz resonator and its application in acoustic metamaterial system. Mech. Syst. Signal Proc. **132**, 595–608 (2019). https://doi.org/10.1016/j.ymssp.2019.07.017
46. Huang, G., Sun, C.: Band gaps in a multiresonator acoustic metamaterial. Int. J. Comput. Sci. (2010). https://doi.org/10.1115/1.4000784
47. Li, Q., He, Z., Li, E.: Dissipative multi-resonator acoustic metamaterials for impact force mitigation and collision energy absorption. Acta Mech. **230**, 2905–2935 (2019). https://doi.org/10.1007/s00707-019-02437-4
48. Krushynska, A.O., Amendola, A., Bosia, F., Daraio, C., Pugno, N.M., Fraternali, F.: Accordion-like metamaterials with tunable ultra-wide low-frequency band gaps. New J. Phys. **20**, 073051 (2018). https://doi.org/10.1088/1367-2630/aad354
49. Xiao, Y., Mace, B.R., Wen, J., Wen, X.: Formation and coupling of band gaps in a locally resonant elastic system comprising a string with attached resonators. Phys. Lett. A **375**, 1485–1491 (2011). https://doi.org/10.1016/j.physleta.2011.02.044
50. Chen, Z., Wang, G., Mao, Y., Lim, C.W.: New metamaterial mathematical modeling of acoustic topological insulators via tunable underwater local resonance. Appl. Math. Model. **108**, 258–273 (2022). https://doi.org/10.1016/j.apm.2022.03.023
51. Gei, M., Movchan, A., Bigoni, D.: Band-gap shift and defect-induced annihilation in prestressed elastic structures. J. Appl. Phys. **105**, 063507 (2009). https://doi.org/10.1063/1.3093694
52. Chen, X., Xu, X., Ai, S., Chen, H., Pei, Y., Zhou, X.: Active acoustic metamaterials with tunable effective mass density by gradient magnetic fields. Appl. Phys. Lett. **105**, 071913 (2014). https://doi.org/10.1063/1.4893921
53. Ghannadiasl, A., Mofid, M.: An analytical solution for free vibration of elastically restrained Timoshenko beam on an arbitrary variable Winkler foundation and under axial load. Lat. Am. J. Solids Struct. **12**, 2417–2438 (2015). https://doi.org/10.1590/1679-78251504
54. Zhou, W., Wu, B., Su, Y., Liu, D., Chen, W., Bao, R.: Tunable flexural wave band gaps in a prestressed elastic beam with periodic smart resonators. Mech. Adv. Mater. Struct. **28**, 221–228 (2019). https://doi.org/10.1080/15376494.2018.1553261
55. Yuan, Y., Zhou, W., Li, J., Chen, W., Bao, R.-h: Tuning bandgaps in metastructured beams: numerical and experimental study. J. Zhejiang Univ.-SCI A **20**, 811–822 (2019). https://doi.org/10.1631/jzus.A1900330
56. Hu, G., Austin, A.C., Sorokin, V., Tang, L.: Metamaterial beam with graded local resonators for broadband vibration suppression. Mech. Syst. Signal Proc. **146**, 106982 (2021). https://doi.org/10.1016/j.ymssp.2020.106982
57. Baz, A.: Active control of periodic structures. J. Vib. Acoust. **123**, 472–479 (2001). https://doi.org/10.1115/1.1399052
58. Chen, Z., Lim, C.W.: Static-dynamic relationship for flexural free vibration of extensible beams. Int. J. Struct. Stab. Dyn. **18**, 1871010 (2018). https://doi.org/10.1142/S0219455418710104
59. Yu, D., Wen, J., Shen, H., Xiao, Y., Wen, X.: Propagation of flexural wave in periodic beam on elastic foundations. Phys. Lett. A **376**, 626–630 (2012). https://doi.org/10.1016/j.physleta.2011.11.056
60. Zhou, W., Chen, W., Destrade, M., Lim, C.W.: Actively controllable topological phase transition in phononic beam systems. Int. J. Mech. Sci. (2020). https://doi.org/10.1016/j.ijmecsci.2020.105668
61. Timoshenko, S.P.: On the correction for shear of the differential equation for transverse vibrations of prismatic bars. Philos. Mag. **41**, 744–746 (1921). https://doi.org/10.1080/14786442108636264
62. Romero-García, V., Sánchez-Pérez, J.V., Castiñeira-Ibáñez, S., Garcia-Raffi, L.: Evidences of evanescent Bloch waves in phononic crystals. Appl. Phys. Lett. **96**, 124102 (2010). https://doi.org/10.1063/1.3367739
63. Xiao, Y., Wen, J., Wen, X.: Flexural wave band gaps in locally resonant thin plates with periodically attached spring-mass resonators. J. Phys. D Appl. Phys. **45**, 195401 (2012). https://doi.org/10.1088/0022-3727/45/19/195401
64. Goffaux, C., Sánchez-Dehesa, J., Yeyati, A.L., Lambin, P., Khelif, A., Vasseur, J., Djafari-Rouhani, B.: Evidence of Fano-like interference phenomena in locally resonant materials. Phys. Rev. Lett. **88**, 225502 (2002). https://doi.org/10.1103/PhysRevLett.88.225502

65. Hsu, J.-C.: Local resonances-induced low-frequency band gaps in two-dimensional phononic crystal slabs with periodic stepped resonators. J. Phys. D Appl. Phys. **44**, 055401 (2011). https://doi.org/10.1088/0022-3727/44/5/055401

Terms and Conditions

Springer Nature journal content, brought to you courtesy of Springer Nature Customer Service Center GmbH (“Springer Nature”).
Springer Nature supports a reasonable amount of sharing of research papers by authors, subscribers and authorised users (“Users”), for small-scale personal, non-commercial use provided that all copyright, trade and service marks and other proprietary notices are maintained. By accessing, sharing, receiving or otherwise using the Springer Nature journal content you agree to these terms of use (“Terms”). For these purposes, Springer Nature considers academic use (by researchers and students) to be non-commercial.
These Terms are supplementary and will apply in addition to any applicable website terms and conditions, a relevant site licence or a personal subscription. These Terms will prevail over any conflict or ambiguity with regards to the relevant terms, a site licence or a personal subscription (to the extent of the conflict or ambiguity only). For Creative Commons-licensed articles, the terms of the Creative Commons license used will apply.
We collect and use personal data to provide access to the Springer Nature journal content. We may also use these personal data internally within ResearchGate and Springer Nature and as agreed share it, in an anonymised way, for purposes of tracking, analysis and reporting. We will not otherwise disclose your personal data outside the ResearchGate or the Springer Nature group of companies unless we have your permission as detailed in the Privacy Policy.
While Users may use the Springer Nature journal content for small scale, personal non-commercial use, it is important to note that Users may not:

1. use such content for the purpose of providing other users with access on a regular or large scale basis or as a means to circumvent access control;
2. use such content where to do so would be considered a criminal or statutory offence in any jurisdiction, or gives rise to civil liability, or is otherwise unlawful;
3. falsely or misleadingly imply or suggest endorsement, approval , sponsorship, or association unless explicitly agreed to by Springer Nature in writing;
4. use bots or other automated methods to access the content or redirect messages
5. override any security feature or exclusionary protocol; or
6. share the content in order to create substitute for Springer Nature products or services or a systematic database of Springer Nature journal content.

In line with the restriction against commercial use, Springer Nature does not permit the creation of a product or service that creates revenue, royalties, rent or income from our content or its inclusion as part of a paid for service or for other commercial gain. Springer Nature journal content cannot be used for inter-library loans and librarians may not upload Springer Nature journal content on a large scale into their, or any other, institutional repository.
These terms of use are reviewed regularly and may be amended at any time. Springer Nature is not obligated to publish any information or content on this website and may remove it or features or functionality at our sole discretion, at any time with or without notice. Springer Nature may revoke this licence to you at any time and remove access to any copies of the Springer Nature journal content which have been saved.
To the fullest extent permitted by law, Springer Nature makes no warranties, representations or guarantees to Users, either express or implied with respect to the Springer nature journal content and all parties disclaim and waive any implied warranties or warranties imposed by law, including merchantability or fitness for any particular purpose.
Please note that these rights do not automatically extend to content, data or other material published by Springer Nature that may be licensed from third parties.
If you would like to use or distribute our Springer Nature journal content to a wider audience or on a regular basis or in any other manner not expressly permitted by these Terms, please contact Springer Nature at

onlineservice@springernature.com